ACS NANO

www.acsnano.org

ARTICLE

Structural and Valence State Modification of Cobalt in CoPt Nanocatalysts in Redox Conditions

Alexandre C. Foucher, Nicholas Marcella, Jennifer D. Lee, Daniel J. Rosen, Ryan Tappero, Christopher B. Murray, Anatoly I. Frenkel, and Eric A. Stach*

Cite This: *ACS Nano* 2021, 15, 20619–20632

Read Online

ACCESS | Metrics & More | Article Recommendations | Supporting Information

ABSTRACT: **Platinum is the primary catalyst for many chemical reactions in the field of heterogeneous catalysis. However, platinum is both expensive and rare. Therefore, it is advantageous to combine Pt with another metal to reduce cost while also enhancing stability. To that end, Pt is often combined with Co to form Co−Pt nanocrystals. However, dynamical restructuring effects that occur during reaction in Co−Pt ensembles can impact catalytic properties. In this study, model Co_2Pt_3 nanoparticles supported on carbon were characterized during a redox cycle with two *in situ* approaches, namely, X-ray absorption spectroscopy (XAS) and scanning transmission electron microscopy (STEM) using a multimodal microreactor. The sample was exposed to temperatures up to 500 °C under H_2, and then to O_2 at 300 °C. Irreversible segregation of Co in the Co_2Pt_3 particles was seen during redox cycling, and substantial changes of the oxidation state of Co were observed. After H_2 treatment, a fraction of Co could not be fully reduced and incorporated into a mixed Co−Pt phase. Reoxidation of the sample increased Co segregation, and the segregated material had a different valence state than in the fresh, oxidized sample. This *in situ* study describes dynamical restructuring effects in CoPt nanocatalysts at the atomic scale that are crucial to understand in order to improve the design of catalysts used in major chemical processes.**

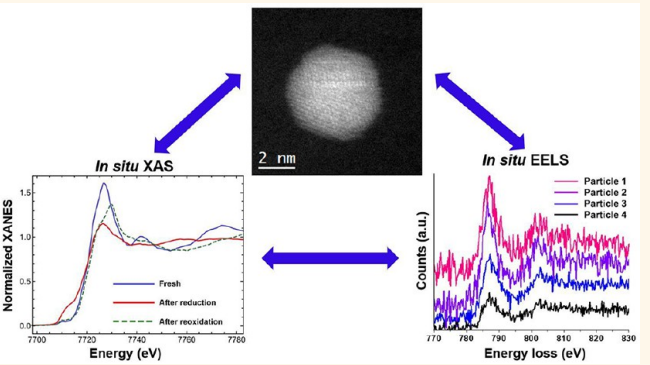

KEYWORDS: *in situ STEM-EELS, in situ XAS, atomic resolution, Co−Pt nanocatalysts, dynamical restructuring effects, bimetallic structures*

Downloaded via BROOKHAVEN NATL LABORATORY on December 29, 2021 at 01:24:38 (UTC).
See https://pubs.acs.org/sharingguidelines for options on how to legitimately share published articles.

Pt-based catalysts are common, as Pt satisfies the Sabatier principle for many reactions.[1−3] As an example, Pt is at the top of the Volcano plot[4,5] for the oxygen reduction reaction (ORR) and the hydrogen evolution reaction (HER). ORR and HER are the reactions used in fuel cells at the cathode and the anode, respectively.[6−10] Other liquid-phase or gas-phase reactions that use Pt as a catalyst include formic acid oxidation,[11] CO oxidation,[12] methanol oxidation,[13] and NO_x reduction.[14] These examples show the wide range of application of Pt as a catalyst. Unfortunately, Pt is one of the most expensive transition metals. To reduce cost, Pt is often combined with another transition metal.[15−17] A Pt-M combination can also be advantageous to control the stability and activity of the catalysts.[18−22] It has been shown that certain crystal surface orientations and stoichiometries can enhance the activity and selectivity of bimetallic catalysts.[23−26] The shape, size, and composition at the nanoscale affect the system's overall catalytic properties, and precise control of those parameters is key to achieving optimal function.[27]

For instance, it has been reported that a mixed solution of Co and Pt is preferable for high activity with the ORR.[28−31] Some studies have focused on Pt_3Co alloys,[32−35] while others indicate that PtCo is an even more efficient catalyst for these same reactions.[36−38] As another example, synergy between Co and Pt has been observed for the conversion of ethane and CO_2 into syngas.[39] In that study, CoPt particles doubled the conversion of ethane and CO_2, compared to its monometallic

Received: October 25, 2021
Accepted: November 10, 2021
Published: November 15, 2021

ACS Publications

© 2021 American Chemical Society

constituents. In the two examples given above, the mixing of Pt and Co allows for a reduced usage of precious Pt. However, the formation of heterogeneities, such as metal segregation within particles, has not been thoroughly investigated under realistic conditions. Dynamical restructuring of Co−Pt structures that are subject to elevated temperatures and either a reductive or oxidative environment is not well understood. This knowledge is crucial as it determines the catalytic properties of the sample while being used for heterogeneous catalysis. For instance, segregation of Co and Pt can be responsible for reduced catalytic properties after cycling.[40,41] Changes in the valence state during reaction impacts the electronic configuration at the sample's surface and ultimately affects absorption and desorption energies for gas molecules.[42] It is known that freshly synthesized Co−Pt particles can have compositional heterogeneities, with partial segregation of Co and Pt.[43−45] Exposure of the Co−Pt system to H_2 or other nonoxidative atmospheres at elevated temperatures has been shown to improve the mixing of Co and Pt, and can lead to the formation of an intermetallic solution.[36,46,47] However, it is not clear whether some Co remains segregated and oxidized during and after annealing. This point is important because incomplete reduction and mixing of Co and Pt will impact the catalytic properties for HER, ORR, or gas-phase reactions. Additionally, reoxidation of Co−Pt should return the sample to a similar configuration as in the fresh sample. However, potential changes in valence state and Co distribution would modify catalytic properties upon usage.

In situ analysis can provide valuable insight into the structural evolution of catalysts. The study of CoPt catalysts under *in situ* conditions is necessary to obtain crucial information about heterogeneous catalysis and cannot be replaced with standard *ex situ* methods. Indeed, the study of metallic catalysts under vacuum at room temperature will be completely different than their structure under a gaseous environment at elevated temperature. This is evident from the Ellingham diagram and the Co−Pt phase diagram in Figure S1.

Here, we utilize a multimodal *in situ* characterization approach to track the dynamical evolution of Co_2Pt_3 nanoparticles supported on an amorphous carbon film. We chose to characterize a random Co_2Pt_3 alloy, as intermetallic solutions have been extensively investigated in previous work.[48,49] We take advantage of recently developed atmospheric pressure electron microscopy methods and extend them to be compatible with synchrotron X-ray probes. We have developed this approach in previous work to characterize other monometallic or bimetallic samples, including Pt, Pd, and Pt−Ni nanoparticles.[50−53] We use this correlative approach here to understand particle structure and oxidation state changes with both X-ray absorption spectroscopy (XAS), including X-ray near-edge spectroscopy (XANES) and extended X-ray absorption fine structure (EXAFS) analysis, as well as with scanning transmission electron microscopy (STEM), electron energy loss spectroscopy (EELS), and energy dispersive X-ray spectroscopy (EDS).

The sample was enclosed in a small microreactor with an inner spacing of 1 μm between two 50 nm Si_3N_4 windows (Figure 1). One of these windows had a heating coil embedded and can raise the temperature up to 1000 °C. The microreactor is then inserted in a dedicated holder that allows a controlled flow of gases. In this study, H_2 and O_2 gases were inserted into the microcell through the holder, and the temperature was elevated up to 500 °C. Hence, this system allowed us to study nanocatalysts in realistic conditions instead of observation under vacuum, as would normally be required in STEM (*e.g., ex situ*).

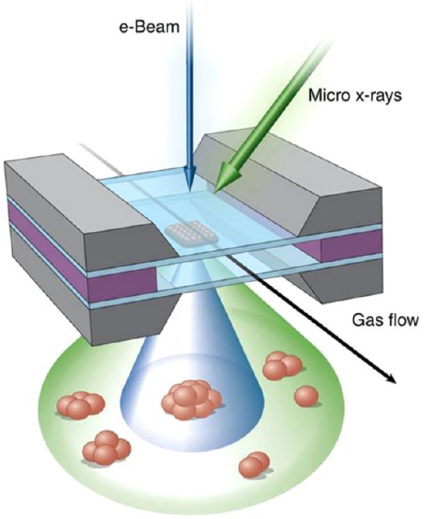

Figure 1. Schematic of the microcell used for *in situ* XAS and *in situ* STEM. The sample is enclosed between two thin Si_3N_4 windows transparent to electrons and X-rays. Gas flows inside the cell thanks to a dedicated *in situ* holder. Temperature is elevated with a microfabricated heating element embedded in one of the windows. Reprinted (adapted or reprinted in part) with permission from ref 50. Copyright 2015 Wiley-VCH.

XAS analysis was performed with a 10 μm beam at the X-ray Fluorescence Microscope (XFM) beamline at the National Synchrotron Light Source II at Brookhaven National Laboratory. This beam size is ideal: it was shown in prior studies[50,52−54] that it is sufficiently large to give a good signal-to-noise ratio while also being small enough to be focused into the viewing window. A larger beam will excite other components in the microcell and ultimately reduce the signal quality. Conversely, a smaller beam will emphasize problems with particle distributions within the microreactor that are not densely packed and thus decrease the X-ray absorption spectrum quality.

RESULTS AND DISCUSSION

The as-synthesized Co_2Pt_3 nanoparticles supported on amorphous carbon were first characterized with *ex situ* TEM and X-ray diffraction. The data indicates that the particles are monodisperse (average size of 3.3 ± 0.3 nm) and are crystalline (Figure S2). Figure 2a,b shows high-angle annular dark-field scanning transmission electron microscopy (HAADF-STEM) images of the sample at low and high magnification. The X-ray diffraction (XRD) data in Figure 2c shows that the particles have the fcc crystal structure [space group #225, $Fm\bar{3}m$]. The peaks for (111) and (200) planes are located at 40.5°and 46.8°, respectively. These values are higher than the expected peak positions for pure Pt (39.8° and 46.5°), indicating the incorporation of Co in a Pt fcc lattice, with a lattice contraction consistent with Vegard's law. The lighter contrast from the atoms located at the particle's outer surface in Figure 2b indicates preferential segregation of Co, as HAADF-STEM is sensitive to atomic number $\sim Z^{1.65}$.[55] It is noteworthy that the segregated Co has a structure that appears to be consistent with the fcc structure of the alloy. This is even though the equilibrium structure for bulk Co at room

https://doi.org/10.1021/acsnano.1c09450
ACS Nano 2021, 15, 20619−20632

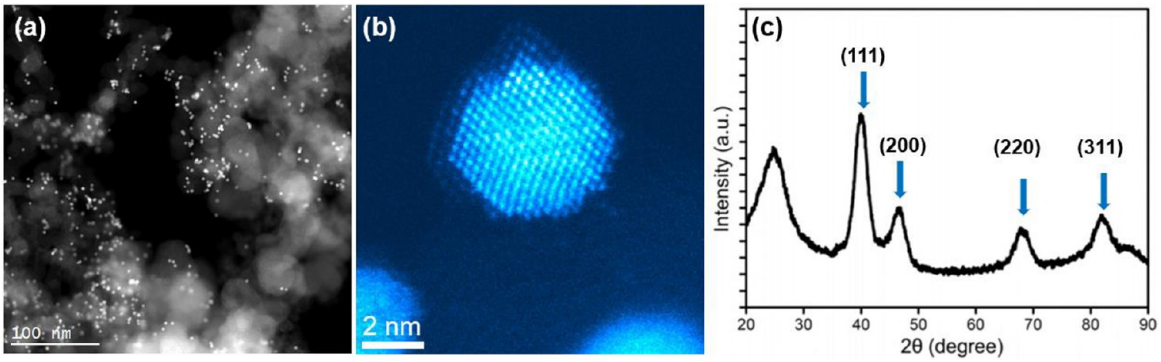

Figure 2. (a). High-angle annular dark-field (HAADF)-STEM image of the sample. Low-magnification images of the nanoparticles supported on a carbon film. (b) False-color HAADF-STEM image showing the atomic structure of an individual Co_2Pt_3 nanoparticle. The lighter atomic contrast on the outer surfaces of the particle is consistent with Co segregation observed with EDS (c) XRD data confirming the crystalline structure of the sample and the incorporation of Co into an fcc Pt lattice, as the peaks are slightly shifted compared to a pure Pt XRD signal, consistent with Vegard's law.

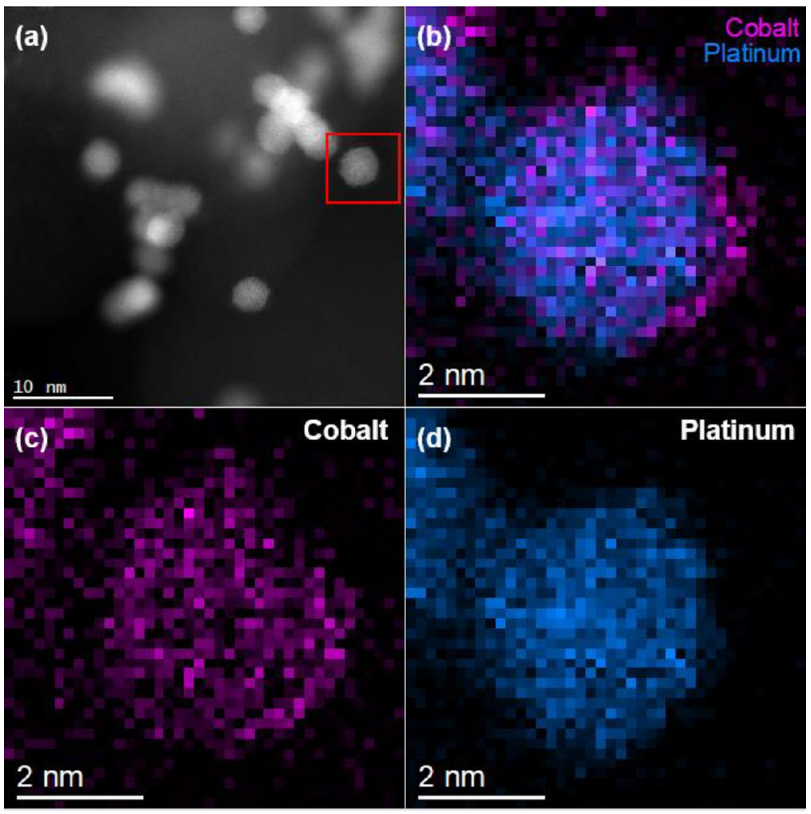

Figure 3. (a) HAADF-STEM image: The red box indicates the region surveyed with EDS. (b) EDS map showing the distribution of Co and Pt within a single Co_2Pt_3 particle. Co is segregated on the surface. Individual elemental maps in (c) and (d) show that the Co and Pt signals overlap, indicating mixed CoPt in the particle bulk.

temperature is hcp [space group 186, $P6_3mc$]. This is consistent with the XRD data in Figure 2c. The spatial distribution of the two transition metals is further characterized by energy-dispersive X-ray (EDS) spectroscopy, shown in Figure 3. Pt and Co are mixed in the particle bulk, but segregation of Co to the surface of the particle is visible, consistent with the HAADF image shown in Figure 2b. Corresponding EDS spectra support this conclusion and are provided in Figure S3. Additional EDS maps of other particles show that Co segregation happens for most particles (Figures S4 and S5). Ideally, a fully mixed solution of transition metals is desired to keep some Pt atoms on the surface of the particles; the Pt can then interact with gases and catalyze chemical reactions.[56] However, segregation of Co in fresh Co–Pt particles has been frequently observed.[57,58,40] Hence, the Co_2Pt_3 sample in this study appears to be broadly representative of typical Co–Pt systems synthesized for catalysis. Partial segregation of Co can be due to the synthesis technique, or it can happen shortly after exposure to air after the synthesis. Segregation of Co is known to be one of the causes of catalyst deactivation during ORR.[59] Indeed, surface segregation of Co can fully cover Pt atoms and ultimately undermine the catalytic potential of the bimetallic system. Additionally, excessive segregation of Co could lead to a

https://doi.org/10.1021/acsnano.1c09450
ACS Nano 2021, 15, 20619–20632

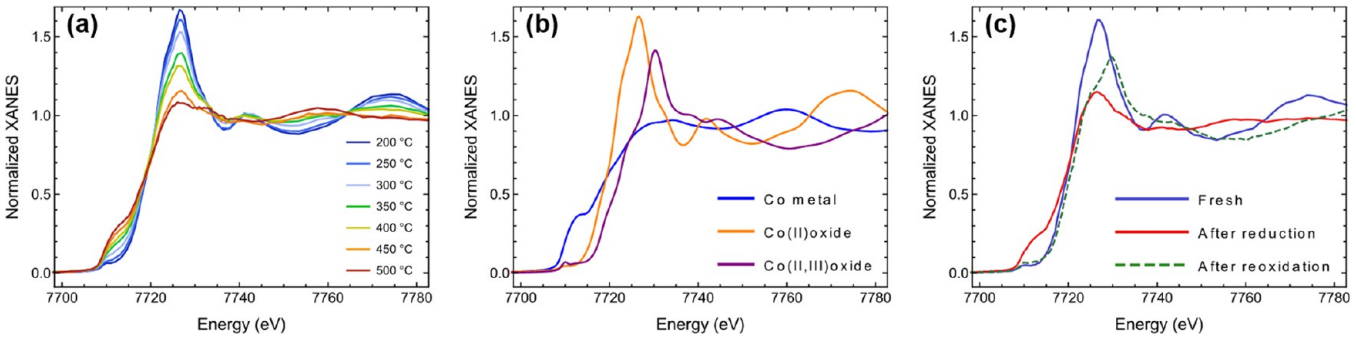

Figure 4. Data from the *in situ* XAS experiment. (a) XAS data from the Co K edge of the fresh sample as it is progressively reduced when the temperature is elevated to 500 °C. XAS spectra were collected after 30 min of exposure to H_2 at the indicated temperature. Although some slight reduction is visible at 200 °C, the desorption of O atoms is accelerated at temperatures above 200 °C. (b) XAS data of reference Co metal and Co oxides. The difference between the reduced sample and Co K edge for metallic Co emphasizes that the sample could not be fully reduced after prolonged exposure to H_2 at 500 °C. (c) XAS data collected for the fresh (oxidized) sample, after reduction at 500 °C, and after reoxidation at 300 °C. The sample was brought back to room temperature under helium, and the data were used for EXAFS analysis. A clear change in the edge shape is visible after reoxidation when the spectra are compared to those of the fresh sample. This indicates a difference in valence state for Co. The edge after reduction at 500 °C in (c) is slightly different from the edge after reduction at 500 °C in (a). In (c), we collected and merged multiple spectra, and the data were then analyzed with EXAFS fits. Additionally, some slight reoxidation happened when the sample was brought back to room temperature.

leaking of transition metals within the fuel cell and damage the membrane in proton-exchange membrane fuel cells (PEMFC).[60,61]

EDS data (Figure S6) of Co_2Pt_3 particles also showed that segregated Co on the particles' surface is oxidized. An *ex situ* STEM-EELS analysis also indicates a few oxidized Co clusters scattered on the carbon surface (Figures S7 and S8).

After this initial *ex situ* TEM analysis, the sample was enclosed in the microreactor for *in situ* studies and analyzed with X-ray absorption spectroscopy (XAS). The experiment was done at a dedicated beamline for X-ray fluorescence microscopy (XFM), and fluorescent X-rays were collected. A microprobe of 10 μm was used to scan the sample while the temperature and the gas environment were modified. The setup enables the analysis of sections of the sample at the micrometer scale and at multiple locations. The specimen was exposed to H_2 and O_2 to simulate reductive and oxidative conditions during reactions. Indeed, it is known that catalysts can be either reduced or oxidized during the catalytic process.[62,63] Even though some reactions such as ORR and HER are performed at room temperature (RT), the sample was studied at elevated temperature to accelerate and amplify the effects of exposure to O_2 and H_2. Hence, the experiment provides an insight into degradation mechanisms occurring after long usage of the nanocatalysts.[64] Additionally, an *in situ* study of the sample under H_2 at elevated temperature describes structural changes during annealing, a crucial step often performed after synthesis to improve the random distribution of Co and Pt.[21,65,66]

The temperature was first elevated to 200 °C under a 100% H_2 atmosphere and subsequently elevated by 50 °C increments every 30 min until a maximum temperature of 500 °C was reached. The temperature was kept at 500 °C for 2 h. Then, the sample was cooled to room temperature in an inert environment using helium, and subsequently exposed to 100% O_2 at a temperature of 100 °C. Again, the temperature was increased by 50 °C every 30 min until reaching a maximum temperature of 300 °C. The temperature was kept at 300 °C for 1 h. The Co K edge at 7708.9 eV was tracked during the redox cycle. It was not possible to also track the Pt edges as the microchip contained components with metallic Pt, whose signal overlapped with the fluorescent X-rays coming from the sample. We performed analysis of the X-ray absorption near-edge structure (XANES) and extended X-ray absorption fine structure (EXAFS).

Figure 4 summarizes the main results of the *in situ* XAS experiment: Figure 4a presents the kinetics of CoPt particle reduction and shows an acceleration of the process for temperatures above 200 °C. The spectra were collected 30 min after exposure to H_2 for temperatures between 200 and 450 °C. At 500 °C, the spectrum was collected after 1 h of exposure to H_2. As compared to the fresh sample, the XANES during and after reduction displayed a decrease in the white line intensity and a negative shift of the edge to the metallic position, which is consistent with the reduction of Co oxides to metallic species. However, on comparison of the reduced samples to metallic Co foil (Figure 4b), there is a broadening of the absorption edge and a larger white line intensity. These effects are likely attributed to the presence of unreduced Co oxide species.

Full reduction could not be achieved, even after prolonged exposure to H_2 at 500 °C. In fact, after 2 h under H_2, it was not possible to see further reduction. Figure S10 shows the Co K edge after 1 h under H_2 and 2 h under H_2 at 500 °C: both spectra are nearly identical. Incomplete reduction of Co at elevated temperature under H_2 has been reported in previous studies.[48] Because the XANES-EXAFS data is obtained from multiple particles at once, it is not possible to determine if Co oxides are present in all particles or only a fraction of them.

Figure 4c shows the Co_2Pt_3 Co K edge before exposure to hydrogen (fresh), after reduction at 500 °C (reduced), and after oxidation at 300 °C (oxidized). All data were collected at room temperature after cooling in He. The XANES is useful for making qualitative conclusions about oxidation state, as the edge position and shape of the edge peak (i.e., white line) are directly related to the electronic structure. The Co_2Pt_3 XANES spectra (fresh, reduced, and oxidized) were compared to spectra collected from Co reference standards (Figure 4b). After oxidation, the edge energy increases, and the white line intensity increases. The spectrum is not identical to the spectrum collected at the beginning of the experiment. The edge energy is slightly higher, and the shape and intensity of

https://doi.org/10.1021/acsnano.1c09450
ACS Nano 2021, 15, 20619−20632

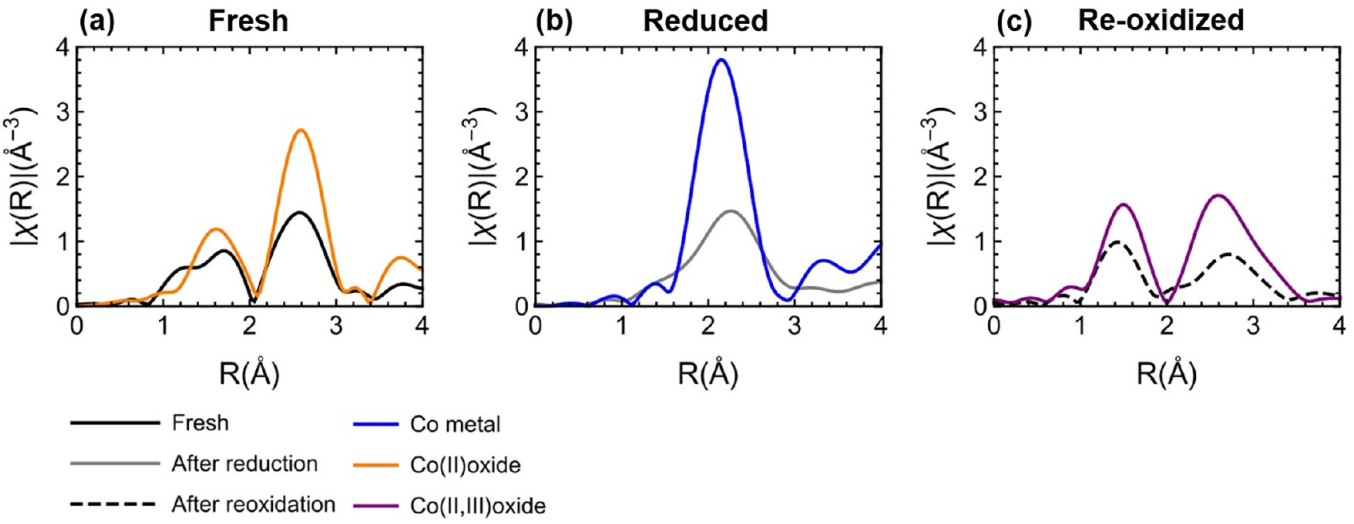

Figure 5. FT-EXAFS collected for the fresh, reduced, and reoxidized sample. The Co K edge was used, and reference signals are also plotted. (a) FT-EXAFS for the fresh sample, suggesting Co(II) oxide is dominant. (b) FT-EXAFS for the reduced sample. The slight shoulder in the plot between 1.5 and 2 Å may be due to Co−O bonding. The reference plot for Co metal suggests that most Co has been reduced. (c) FT-EXAFS for reoxidized sample. A split is visible as Co−O and Co−Co bonds are present. Co(II,III) seems to be the dominant species as the reference plot overlaps well with the experimental data.

Table 1. Best EXAFS Fitting Parameters: Coordination Numbers *N*, Interatomic Distances *R*, and Debye−Waller factors σ^2[a]

state	$N_{(Co-Co)}$	$N_{(Co-O)}$	$R_{(Co-Co)}$	$R_{(Co-O)}$	$\sigma^2_{(Co-Co)}$	$\sigma^2_{(Co-O)}$
Fresh	10 (2)	2.3 (5)	3.00 (1)	2.11 (1)	0.014 (2)	0.002 (3)
Reduced	5 (2)	1.1 (7)	2.56 (2)	2.08 (5)	0.011 (4)	0.011 (4)
Oxidized	7 (3)	0.9 (4)	3.33 (1)	1.94 (2)	0.009 (3)	0.002 (4)
		8 (2)		3.46 (3)		0.009 (3)

[a]The uncertainties in the last significant digits are shown in parentheses. For the oxidized sample, first-shell oxygens (top) and second-shell oxygens were fitted.

the white line are different. Upon comparing the XANES in the oxidized state to Co oxide references, we find that Co has a valence state similar to Co_3O_4 (Figures 4b and S9). In contrast, the majority of the Co in the fresh Co_2Pt_3 sample is in the +2 oxidation state, as the edge position and shape are almost identical to that seen in CoO (Figures 4b and S9).

Figure 5 presents the Fourier Transform magnitude EXAFS (FT-EXAFS) collected from the fresh, reduced, and oxidized sample at room temperature. The plots are also compared with the FT-EXAFS of reference samples, to underline the dominant Co species after each step.

The fresh and oxidized sample feature a short-distance metal−nonmetal peak (likely due to Co−O bonds in the first nearest-neighbor shell), and a long-distance metal−metal peak (Co−M; M is Co and/or Pt, in the second nearest-neighbor shell). In the oxidized sample, the Co−M peak is split: that may be explained by the mixing of metallic and oxidized Co species. After reduction, there is only one metal−metal peak, which is located approximately at the metallic Co position, as evident from comparison to the FT-EXAFS Co foil. The Co−M peak has a slight shoulder between 1.5 and 2 Å that may be due to Co−O bonding. The position in the Co−M peak is less than expected for an alloy of 40% Co in Pt and, thus, may indicate a lack of Co mixing with Pt. EXAFS fitting will be used *vide infra* to quantify the contributions to the metal and nonmetal peaks.

For quantitative analysis, conventional EXAFS fitting can be employed to parametrize the EXAFS oscillations in terms of local structural parameters. Indeed, Co_2Pt_3/C is a complex system with many bonds that could be modeled, such as Co−Co, Co−O, Co−Pt, Co−C, and Pt−C. It is not possible to fit the EXAFS data with a model that encompasses all possible bonds, hence the need to narrow down the starting model with other experimental characterization. The *ex situ* STEM data provided evidence of bulk Co, segregated to the surface of the particles. Additionally, EXAFS analysis with a limited number of bonds involving Co oxides and a Co−Pt alloy did not yield successful results. To simplify the EXAFS modeling, the data were fitted with a combination of Co species. With this approach, the EXAFS data were successfully fitted, and the best models are provided in this work.

The EXAFS data in Figure 4c were fit with a nonlinear least-squares fitting approach employed by the Artemis program (details in SI). The best-fit parameters are summarized in Table 1 and underline the significant differences of the EXAFS data upon reduction and oxidation. Table 2 provides the species that were the best fits for the data. The fitted plots in *k*-

Table 2. Summary of Best Fits after EXAFS Analysis of the *in Situ* Data

sample	dominant Co oxide(s) based on XANES-EXAFS analysis
Fresh	CoO
Reduced under H_2 at 500 °C	Co and CoO
Reoxidized under O_2 at 300 °C	Co_3O_4

https://doi.org/10.1021/acsnano.1c09450
ACS Nano 2021, 15, 20619−20632

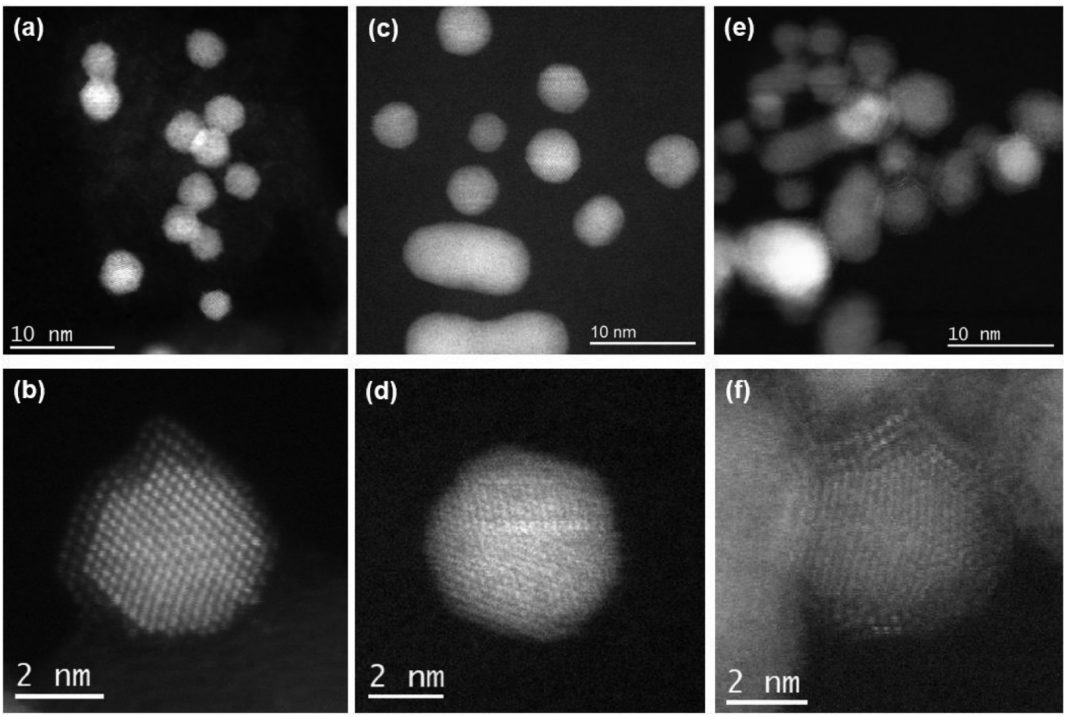

Figure 6. *Ex situ* and *in situ* atomic resolution images of Co_2Pt_3 particles during the redox cycle. (a,b) Atomic resolution HAADF-STEM images (*ex situ*) of fresh Co_2Pt_3 particles showing partial segregation of Co to the edges of the particles. (c,d) Atomic resolution HAADF-STEM images (*in situ*) of Co_2Pt_3 particles after reduction at 500 °C. No region of lighter atomic contrast is observed on the surface, indicating an improved mixing of Co and Pt. (e,f) Atomic resolution HAADF-STEM images (*in situ*) of CoPt particles after oxidation at 300 °C. A shell of Co oxide is observed on all particles. The crystal structure is different in the shell than in the core. Additionally, EELS data (Figure 7) indicate the oxidation of cobalt.

and *R*-space are shown in the Supporting Information (S11). In the fresh sample, the coordination numbers (CNs) of Co−O (2.3 ± 0.5) and Co−Co (10 ± 2) are close to what is expected for bulk CoO (Co−O = 4 and Co−Co = 12). This is surprising, as the *ex situ* STEM images showed only a slight segregation of Co in the fresh sample. Nevertheless, the EXAFS fit underlines the presence of segregated Co with CoO as the dominant species, consistent with our *ex situ* STEM observations.

After reduction, the CN for Co−Co bonds is lower. This shows better incorporation of Co with Pt upon exposure to H_2 at elevated temperature, consistent with previous observations in the literature.[66] It is also interesting to notice the incomplete reduction of Co, as Co−O bonds (1.1 ± 0.7) could be detected after exposure to H_2 at 500 °C.

The sample is then quickly reoxidized to a valence state similar to Co_3O_4 upon exposure to pure oxygen. The average CN for Co−O and Co−Co bonds increases upon reoxidation, indicating segregation of cobalt. However, the CN for Co−Co bonds remains well below 12, suggesting that the segregated Co volumes have a relatively limited size. Hence, it is reasonable to assume large regions in the sample where Co and Pt remain partially mixed even after reoxidation. Indeed, if Co were fully segregated, it should have a CN close to 12, as most Co atoms inside the bulk would have 12 Co nearest neighbors (see Table S1 for local parameters for bulk Co references). However, it is difficult to know from the EXAFS data the magnitude of Co segregation upon reoxidation of the sample. Indeed, the Co−Co coordination number increased to an average of 7 for the Co_3O_4 phase. In contrast, it was 5 for Co−Co bonds in CoO. However, the spatial distribution of oxides within the sample cannot be known, solely based on XANES-EXAFS analysis. Additionally, changes in morphology are difficult to track with XAS for a complex system. Finally, the 10 μm X-ray beam provides representative data for thousands of particles, and it is impossible to determine the dynamic restructuring effect for individual particles. Hence, *in situ* XAS offers valuable insight into the sample at the micron level, but it is not possible to determine phenomena at the nanoscale.

To summarize, XANES-EXAFS indicates changes in the valence state of Co during the redox cycle. As expected, the oxidation number of Co is lowered upon reduction, although some oxides remain. After reoxidation, cobalt has a higher oxidation level than at the beginning of the experiment. EXAFS fitting suggests the presence of a CoO oxide at the beginning and a Co_3O_4 oxide after reoxidation. Previous studies indicate that formation of a Co_3O_4 phase after oxidation at 300 °C is thermodynamically possible.[67−69] The analysis of the coordination number for Co−O bonds in the oxide regions detected by EXAFS indicates an increase in the overall amount of oxidized cobalt compared to the fresh sample. However, the morphology and distribution of spatial heterogeneities remain unknown.

In order to investigate how restructuring occurs at the nanometer to atomic scale, an *in situ* STEM-EELS experiment was performed. The sub-Å resolution of the electron beam allows us to characterize individual particles at the atomic scale. EDS and EELS data provide chemical information, and HAADF-STEM images visually track changes in morphology and the formation of heterogeneity within the particles.

https://doi.org/10.1021/acsnano.1c09450
ACS Nano 2021, 15, 20619−20632

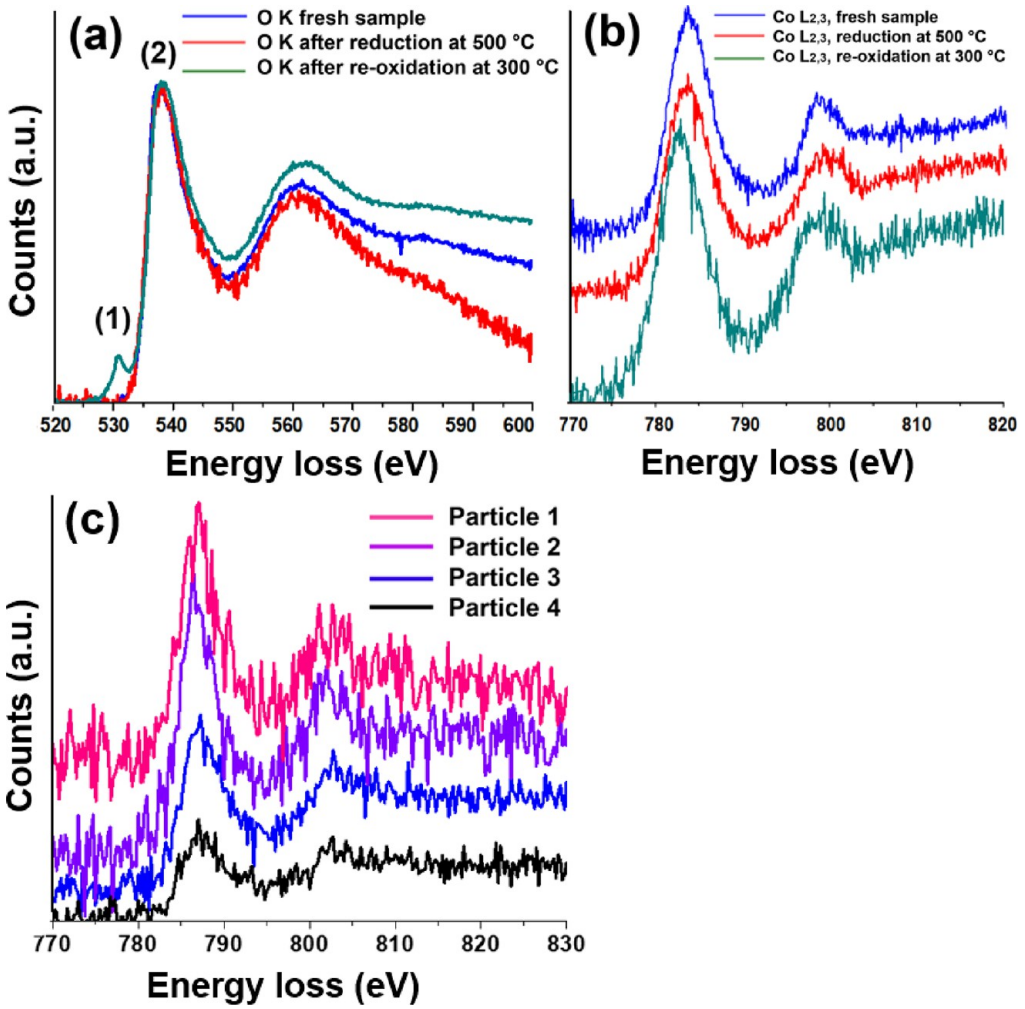

Figure 7. ***In situ*** **EELS analysis of the sample. (a) O K EELS edge of 30−40 particles in the fresh sample, after reduction at 500 °C and after reoxidation at 350 C. The signal is from both the sample and the cell's windows. The appearance of a pre-edge feature upon reoxidation is exclusively from the sample. It indicates the formation of a highly oxidized phase that was not present at the beginning of the experiment. (b) Co $L_{2,3}$ EELS edge of 30−40 particles in the fresh sample, after reduction at 500 °C and after reoxidation at 350 C. The observed increase of the L_3/L_2 ratio indicates the reduction of Co. The observed increase of the L_3/L_2 ratio indicates oxidation of Co. (c)** ***In situ*** **EELS analysis of individual particles after reduction at 500 °C. No major change in either shape or L_3/L_2 ratio was observed, indicating a uniform reduction of individual particles in the sample.**

The same microreactor setup was used in a transmission electron microscope operating in STEM mode (JEOL NEOARM). Also, the same experimental procedure was performed after fresh samples were loaded into the reactor: exposure to H_2 at the same temperature ramp to 500 °C followed by reoxidation under O_2 at 300 °C. The EELS spectra of O K (529 eV loss) and Co $L_{2,3}$ edges (779 eV loss for L_3, 794 eV loss for L_2) were tracked during the high-temperature gas exposures. The Pt $M_{4,5}$ edges (2122 eV for M_5 and 2202 for M_4) were also obtained (Figure S12). In order to obtain the EELS spectra, the cell was purged with N_2 to eliminate the contribution of gaseous oxygen to the spectra.

Figure 6 shows atomic resolution HAADF-STEM images demonstrating structural changes within particles after reduction at 500 °C and reoxidation at 300 °C. It was not possible to observe segregated Co after reduction, in contrast to the observations in the fresh sample: no regions in the particles with light atomic contrast could be identified. After reoxidation at 300 °C, substantial segregation of Co was observed with the formation of a core−shell structure (Figure 6e and f). In Figure 6f, it is possible to see a different atomic arrangement for the shell than for the core, indicating a difference in crystal structure. One can assume that the shell is mostly Co_3O_4 [space group #227, $Fd\bar{3}m$] and the core remains a Co−Pt random alloy [space group #225, $Fm\bar{3}m$]. Subsequent EELS analysis revealed the presence of oxygen in the sample, consistent with the conclusion that the shell is composed of Co oxides. It is interesting to notice that Co oxide appears to fully enveloping the Co−Pt core from this image orientation. Hence, reoxidation leads to increased segregation of Co to the surface compared to the fresh sample, with Pt mainly confined in the core. Thus, it can be expected that the sample will have inferior catalytic activity for reactions catalyzed by Pt after exposure to oxygen.

The chemistry of the sample was investigated with EELS. Figure 7 shows the O K edge and the Co $L_{2,3}$ edge at the beginning of the *in situ* analysis, after reducing 2 h at 500 °C and after oxidation for 1 h at 300 °C. The cell was purged with nitrogen before every EELS measurement. To collect the O K edge, a single EELS map was performed on a group of 30 to 40

https://doi.org/10.1021/acsnano.1c09450
ACS Nano 2021, 15, 20619−20632

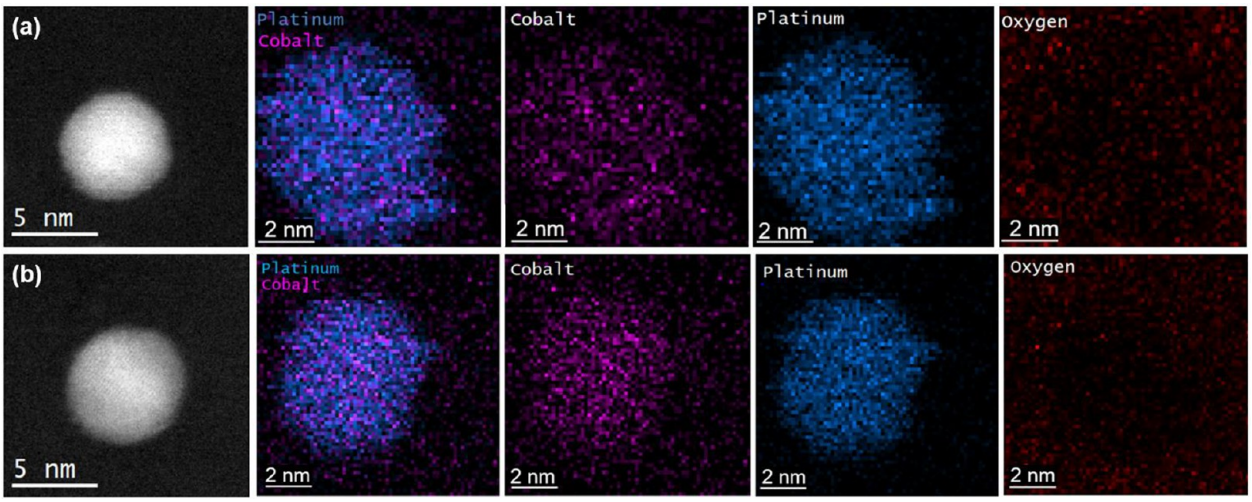

Figure 8. EDS analysis of two isolated particles after reduction at 500 °C. (a) First particle with EDS spectra for Co, Pt, and O. No oxygen signal could be detected from the particles and uniform mixing between Co and Pt was achieved. (b) Analysis for a second particle underlining that the particle shown (a) is not an outlier.

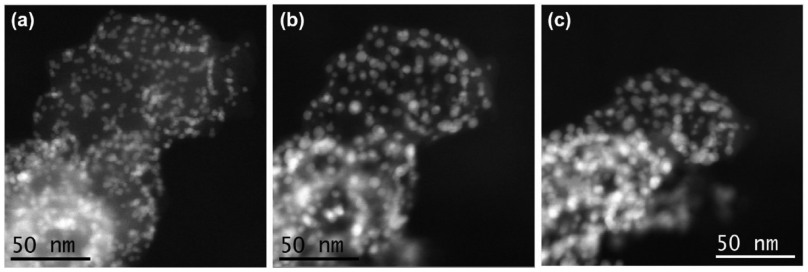

Figure 9. Particle migration and coalescence during reduction at elevated temperature. The exposure to heat explains the formation of clusters of particles observed. These aggregates are more difficult to reduce than isolated particles. (a) Co_2Pt_3 particles supported on C at 100 °C. (b) Same region after 30 min exposure to H_2 at 500 °C. (c) Same region after 90 min exposure at 500 °C.

particles on the amorphous carbon support in order to obtain high signal intensity. The O K edge is a relevant parameter to track during *in situ* analysis as it contains many subtle features that can help distinguish electronic configuration in transition metals. In this study, the O K signal arises from both the oxygen contained in the Co−Pt sample (Figure S4) and the windows of the microcell. Indeed, the Si_3N_4 windows contain traces of SiO_2. The O K edge of the windows, without any sample or gaseous oxygen in the cell, is shown in Figure S13. The spectra did not change during the experiment, indicating that the SiO_2 phase was unmodified during the redox cycle. Hence, changes in the collected O K edge, resulting from the sample and the windows, are exclusively attributed to the shifts in oxidation state in the sample.

In Figure 7a, it is possible to see the appearance of a pre-edge peak (1) upon reoxidation of the sample. This indicates that the particles are more oxidized after reoxidation than at the beginning of the experiment. This observation is consistent with the *in situ* EXAFS analysis.[70] Indeed, the pre-edge peak (1) corresponds to transitions from the O 1s state to a hybridized state of O 2p and 3d orbitals in heavily oxidized transition metals (above +2).[70] Previous work also indicates that Co with a low oxidation state does not display a prepeak feature for the O K edge.[71−73] Thus, we can conclude the formation of a highly oxidized phase upon reoxidation of the sample that was not present in the fresh sample. The only stable candidate for a Co phase with higher oxidation state than CoO would be Co_3O_4. The other potential candidate would be Co_2O_3, but it is unstable and tends to decompose into other Co oxides, including Co_3O_4.[74] Additional sources also indicated the stability of Co_3O_4 under O_2 at elevated temperature (Figure S14). The EXAFS data are consistent with this conclusion.

Maps collected from a large group of particles indicate the presence of the pre-edge feature for a large majority of particles. However, some particles did not display the prepeak, indicating that there are spatial heterogeneities in the valence states upon reoxidation (Figure S15).

The $L_{2,3}$ edges of Co at 779 and 794 eV were also analyzed. As with the O K edge, a group of 30 to 40 particles was analyzed to collect sufficient signal. The L_3/L_2 ratio for Co changes very modestly in these experiments. It is higher for the reduced sample (the ratio is 1.55) and slightly lower when oxidized (the ratio is 1.42). This is consistent with previous publications, as metallic Co should exhibit a higher L_3/L_2 ratio than oxidized Co.[75−77] Additionally, oxidized Co has a deeper trough between L_3 and L_2 than metallic Co, which is also evident in the spectra of Figure 7b. Thus, the EELS data indicate effective reduction of Co upon exposure to H_2 at 500 °C, as expected, and it is consistent with the XANES results discussed above.

To determine local heterogeneities in the valence state between Co_2Pt_3 particles after reduction, we performed *in situ* EELS analysis of the Co $L_{2,3}$ edge of individual and isolated particles. Figure 6c shows the EELS spectra of four particles. There are no substantial changes in the shape or L_3/L_2 ratio

https://doi.org/10.1021/acsnano.1c09450
ACS Nano 2021, 15, 20619−20632

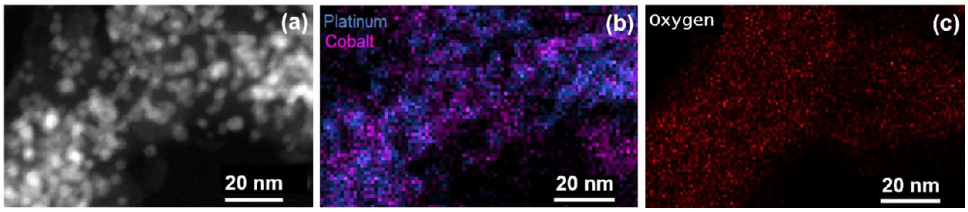

Figure 10. *In situ* STEM analysis from a cluster of particles after reduction at 500 °C for 2 h. (a) *In situ* imaging of the region surveyed for EELS and EDS analysis after the reaction. (b) Combined EDS maps of Co and Pt after reduction: a certain level of Co segregation is observed. (c) EDS map of oxygen underlines the presence of O in clusters of particles after reduction at 500 °C. EELS confirms the presence of oxygen. The XANES-EXAFS analysis suggested the presence of oxides after reduction. STEM-EDS/EELS analysis shows that oxides are not present in isolated particles but form during the aggregation of particles during the experiment.

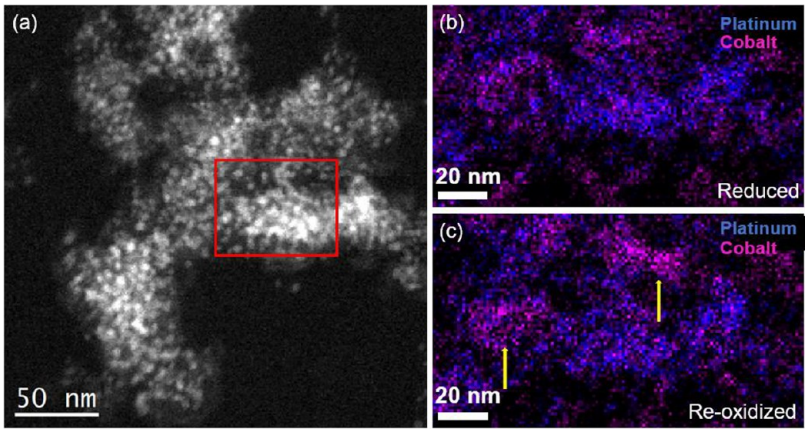

Figure 11. STEM-EDS analysis of a region containing a large number of Co_2Pt_3 particles, after reduction at 500 °C and after reoxidation at 300 °C. (a) HAADF-STEM image of the analyzed region with the red box indicating where EDS was performed. (b) Combined EDS maps of Pt and Co after reduction at 500 °C. Both transition elements are partially mixed and partially segregated as the intensity of the Co and Pt signals does not overlap perfectly. (c) Combined EDS maps of Pt and Co after reoxidation at 300 °C. A stronger EDS signal for Co appears for the two regions indicated by the yellow arrows. It shows segregation of Co that would have been difficult to conclude solely based on a XANES-EXAFS analysis. The Co regions appear to be relatively large and could only be found in areas with aggregates of particles.

between the particles. This indicates that the reduction of Co in isolated CoPt particles is broadly uniform. Furthermore, EDS maps were obtained on particles 3 and 4 (Figure 8) and indicated no significant presence of oxygen. The corresponding EELS maps for the O K edge are provided in Figure S16 and also do not show the presence of oxygen. Additionally, it was possible to see a uniform mixing of Co and Pt, with no segregation of Co on the edges.

To conclude, reduction affects isolated Co_2Pt_3 particles in a similar way: full reduction was achieved, and no segregation of Co was observed.

Since the EXAFS data suggest the presence of cobalt oxides even after reduction at 500 °C, multiple areas were investigated with EELS, and oxygen could be detected on clusters of particles. Indeed, the exposure of the sample to elevated temperature favored particle migration and coalescence (PMC), leading to aggregates of particles, as shown in Figure 9. Exposure to elevated temperatures leads to PMC and aggregation of particles in areas initially containing a large number of particles.

An EDS analysis of another similar region showed the presence of oxygen as well as segregation of Co and Pt (Figure 10). The presence of oxygen is also confirmed by an EELS map (Figure S17). Hence, it is possible to reconcile the EELS data with the XANES-EXAFS analysis: for isolated particles, it was not possible to detect oxygen or segregation of Co after reduction at 500 °C. However, the coalescence of particles and the formation of clusters on the carbon support can prevent the complete reduction of Co and its incorporation into a Co−Pt random alloy. STEM-EELS analysis revealed morphological and compositional heterogeneities at the nanoscale that explain and complement the XANES-EXAFS analysis.

In addition, XANES-EXAFS suggested segregation of Co upon reoxidation. This can be seen on individual particles (Figure 6), but it is also a phenomenon observed for clusters of particles. *In situ* EDS on aggregated particles shows substantial segregation of Co upon reoxidation of the sample (Figure 11). A map collected from a 120 nm × 60 nm area detects a strong signal for two clusters of Co formed after reoxidation (yellow arrows). It shows that Co migrates outside the mixed Co−Pt phase and forms larger volumes of cobalt-rich phase. The coalescence of particles and formation of larger regions of Co shown in Figure 10c is likely an irreversible process and would be expected to degrade the performance of Co−Pt catalysts. Figure S18 shows further evidence of Co "leaking" outside the CoPt particles. If pure Co particles are formed, separated from the CoPt particles, then the process is very likely irreversible. Additionally, large volumes of cobalt may envelop Pt. Hence, the segregation of cobalt and platinum destroys the desired bimetallic configuration, which requires Pt atoms to be well distributed on the surface.

Thus, we identified two phenomena preventing the optimization of Pt in Co−Pt systems after exposure to O_2 at elevated temperature: first, the formation of a core−shell structure, as shown in Figure 6, and second, coalescence of particles followed by formations of large regions of oxidized Co

https://doi.org/10.1021/acsnano.1c09450
ACS Nano 2021, 15, 20619−20632

as shown in Figure 10. This observation would have been challenging to deduce from the XANES-EXAFS results: the variety of Co phases (metallic, oxides, Co−Pt solutions) makes it difficult to conclude this solely based on EXAFS data. Hence, STEM-EELS/EDS is a complementary technique to XAS and is relevant to achieve a comprehensive understanding of the catalyst at multiple length scales.

CONCLUSION

We have utilized two complementary experimental approaches—*in situ* XAS and STEM—to characterize the dynamic restructuring that occurs in supported bimetallic Co−Pt nanoparticles during reduction and oxidation. After exposure to H_2 at 500 °C for 2 h, XAS analysis (XANES and EXAFS) shows that Co cannot be fully reduced. The STEM-EELS analysis confirms this and shows that Co remains oxidized in clusters of particles, with some coalescence of bulk Co. In contrast, small and isolated particles could be fully reduced after the same treatment and had no additional segregated Co. After exposure to O_2 at 300 °C for 1 h, the valence state of Co was not the same as in the fresh sample. XANES-EXAFS and STEM-EELS analysis suggests the presence of Co_3O_4. Additionally, segregation of Co within particles and in clusters of particles was observed during the process. HAADF-STEM showed that the shell of the particles is mostly Co oxide, reducing the desirable exposure of Pt atoms on the surface. This study demonstrates that the advent of recent *in situ* methods, high-brightness and focused X-ray sources, aberration-corrected TEM, and direct electron detection cameras enables the multimodal study of bimetallic catalysts with high precision.[78,79] Furthermore, the use of complementary, multimodal experimentation allows a deeper understanding of the heterogeneities present in catalysts subject to reaction conditions. These experimental methods allow the design of more active, selective, and stable structures for heterogeneous catalysis.[80,81]

EXPERIMENTAL METHODS

Synthesis. Co_2Pt_3 NPs are synthesized based on a previously reported method.[48] Platinum(II) acetylacetonate (0.67 mmol, Acros Organics, 98%) was dissolved in a solution of oleylamine (41 mL, Sigma-Aldrich, 70%) and 1-octadecene (16 mL, Acros Organics 90%). The reaction mixture was kept at 80 °C for 30 min under vacuum and then heated to 300 °C under a nitrogen atmosphere. Dicobalt octacarbonyl (0.3 mmol, $Co_2(CO)_8$, Acros Organics, 95%) was dissolved in 3.2 mL 1,2-dichlorobezene (Acros Organics, 99%) and injected into the reaction mixture at 170 °C. The reaction mixture was heated to 300 °C at a rate of 10 °C/min. After 30 min, the reaction mixture was cooled to room temperature. The resulting NCs were then purified by precipitation with ethanol and centrifugation at 8000 rpm for 3 min. The precipitate was washed three times with hexane/ethanol (1:3) mixtures and the final NCs were dispersed in hexane. To prepare Co_2Pt_3/C, the as-synthesized NPs, dispersed in hexane, were mixed with carbon powder (Cabot, Vulcan XC72R) to a loading of 10 wt % metal. After sonication for 1 h, the solution was centrifuged at 8000 rpm for 1 min. The supernatant was removed, and the precipitate was washed twice with acetone, followed by centrifugation. After drying each sample in a vacuum oven overnight at 50 °C, the samples were first treated with an O_2 plasma cleaner (Harrick Plasma) for 15 min, then transferred for 1 min into a muffle furnace that had been preheated to 500 °C to remove surface ligands.[48]

Transmission Electron Microscopy. Scanning transmission electron microscopy (STEM) was performed with an aberration-corrected JEOL NEOARM, operating at 200 kV. A condenser lens aperture of 40 μm was used. For imaging and EDS, a camera length of 4 cm and a probe current of 150 pA were used. For EELS, a camera length of 2 cm and a probe current of 500 pA were used. For EELS spectra in Figure 7c, the probe current was elevated to 1000 pA. EELS data were collected with a Gatan K2 camera, a direct-detection camera, to obtain the best signal-to-noise ratio (SNR). A GIF aperture of 5 mm was used, and the energy dispersion was 0.25 eV for all EELS data. For *in situ* studies (XAS, EELS), an environmental holder for gas-heating experiments manufactured by Hummingbird Scientific was used. The sample was enclosed in a microchip made of two 50 nm Si_3N_4 windows. The lower window contains a heating coil to elevate the temperature inside the cell. The mass flow of gases was controlled with a gas system and a software provided by Hummingbird scientific. The flow rate was 5 sccm at all experiments were carried out under 1 bar. For the *in situ* experiment, the temperature was increased by 50 °C every 30 min and ultimately kept at 500 °C for 2 h. All EELS data were taken at the indicated temperature, and the cell was purged with N_2.

EDS and EELS can be performed simultaneously during the STEM *in situ* analysis. Generally, the use of atmospheric pressure gas holders leads to a decrease in the signal-to-noise ratio (SNR) and a reduction in the image resolution. However, in this study, we have used a both a fifth-order optimized, probe-corrected STEM (JEOL NEOARM) and direct electron detection camera (Gatan K2-IS) at the end of the EELS spectrometer to enhance our signal-to-noise, compensating for the impact of the deleterious scattering of electrons by the two Si_3N_4 windows.[78] *In situ* EDS was also improved through the use of two large-area silicon drift detectors,[82] and by slightly tilting the holder to maximize the X-rays counts on the detectors located above the sample.[83] Long exposure to the electron beam was avoided to limit beam-induced effects. Indeed, the amorphous carbon as well as the cobalt were particularly sensitive to prolonged imaging and spectroscopy analysis. Hence, we limited the time of EDS/EELS acquisition on each area to provide accurate and representative results. Several regions and many particles were analyzed to ensure that the observed dynamical restructuring effects were exclusively the results of the environment exposure and no electron irradiation.

Figures S19 and S20 provides additional evidence of the necessity to perform an *in situ* diagnostic of this sample. Exposure to air leads to reoxidation of cobalt and formation of oxygen-rich structures on the carbon film supporting the particles. Thus, it is not possible to treat the particles in a reactor, collect the sample, and perform an *ex situ* analysis, as exposure to air will modify the sample.

X-ray Fluorescence Microscopy. XFM was performed at Brookhaven National Laboratory (BNL) at the 4-BM (XFM) beamline of NSLS-II. The Co K edge (7709.8 eV) was measured with the sample enclosed in the microchip and the environmental holder provided by Hummingbird Scientific. The gas flow was controlled with a mass flow controller and set to 5 sccm. All *in situ* data were obtained with a pressure of 1 bar. XFM data were plotted and analyzed with the Athena/Artemis of the Demeter Package. The amplitude reduction factor So^2 was 0.875, and all data were collected in fluorescence mode. The beam size was 10 μm and was monochromated by an Si(111) crystal pair. The energy range of the beamline was 4−20 keV. For the *in situ* experiment, the temperature was increased by 50 °C every 30 min and ultimately kept at 500 °C for 2 h. XANES data (Figure 4a) were taken at the indicated temperature, under H_2 exposure. For EXAFS analysis (Figures 4c and 5), the sample was cooled to room temperature and the cell was purged with helium before data collection.

ASSOCIATED CONTENT

Supporting Information

The Supporting Information is available free of charge at https://pubs.acs.org/doi/10.1021/acsnano.1c09450.

Additional STEM images, EELS and EDS data; additional XANES and EXAFS data; phase diagram for

https://doi.org/10.1021/acsnano.1c09450
ACS Nano 2021, 15, 20619−20632

Co−Pt; Elligham diagram for Co; NIST data about Co and its oxides; details about EXAFS analysis (PDF)

AUTHOR INFORMATION

Corresponding Author

Eric A. Stach − *Department of Materials Science and Engineering and Laboratory for Research on the Structure of Matter, University of Pennsylvania, Philadelphia, Pennsylvania 19104, United States;* orcid.org/0000-0002-3366-2153; Email: stach@seas.upenn.edu

Authors

Alexandre C. Foucher − *Department of Materials Science and Engineering, University of Pennsylvania, Philadelphia, Pennsylvania 19104, United States;* orcid.org/0000-0001-5042-4002

Nicholas Marcella − *Department of Materials Science and Chemical Engineering, Stony Brook University, Stony Brook, New York 11794, United States;* orcid.org/0000-0002-2224-532X

Jennifer D. Lee − *Department of Chemistry and Chemical Biology, Harvard University, Cambridge, Massachusetts 02138, United States; Department of Chemistry, University of Pennsylvania, Philadelphia, Pennsylvania 19104, United States*

Daniel J. Rosen − *Department of Materials Science and Engineering, University of Pennsylvania, Philadelphia, Pennsylvania 19104, United States;* orcid.org/0000-0003-1463-7363

Ryan Tappero − *Photon Sciences Department, Brookhaven National Laboratory, Upton, New York 11973, United States*

Christopher B. Murray − *Department of Materials Science and Engineering and Department of Chemistry, University of Pennsylvania, Philadelphia, Pennsylvania 19104, United States*

Anatoly I. Frenkel − *Department of Materials Science and Chemical Engineering, Stony Brook University, Stony Brook, New York 11794, United States; Division of Chemistry, Brookhaven National Laboratory, Upton, New York 11973, United States;* orcid.org/0000-0002-5451-1207

Complete contact information is available at: https://pubs.acs.org/10.1021/acsnano.1c09450

Author Contributions

A.C.F. wrote the primary manuscript. E.A.S. and A.I.F. supervised this project and edited the manuscript. J.D.L. and D.R. synthesized the particles under supervision of C.B.M. A.C.F., N.M., and R.V.T. collected the XFM data. A.C.F. conducted STEM-EELS analysis. N.M. and A.C.F. performed the EXAFS fitting under supervision of A.I.F.

Notes

The authors declare the following competing financial interest(s): One of the authors (E.A.S.) has an equity interest in Hummingbird Scientific.

ACKNOWLEDGMENTS

This work was primarily supported as part of the Integrated Mesoscale Architectures for Sustainable Catalysis (IMASC), an Energy Frontier Research Center funded by the U.S. Department of Energy, Office of Science, Basic Energy Sciences under Award #DE-SC0012573. This research used 4-BM (XFM) beamline of the National Synchrotron Light Source, a U.S. DOE Office of Science User Facility operated for the DOE Office of Science by Brookhaven National Laboratory (BNL) under Contract No. DE-SC0012704. This work was carried out in part at the Singh Center for Nanotechnology, which is supported by the NSF National Nanotechnology Coordinated Infrastructure Program under grant NNCI-2025608. Additional support to the Nanoscale Characterization Facility at the Singh Center has been provided by the Laboratory for Research on the Structure of Matter (MRSEC) supported by the National Science Foundation (DMR-1720530). Nanoparticle synthesis and preparation was supported as part of the Catalysis Center for Energy Innovation, an Energy Frontier Research Center funded by the U.S. Department of Energy, Office of Science, Office of Basic Energy Sciences under Award Number DE-SC0001004. The authors would like to thank H. T. Ngan, G. Yan and P. Sautet for providing the stability diagram of Co oxides in Figure S12. The authors also would like to thank S. Nicholas for her help at the 4-BM beamline.

REFERENCES

(1) Stacy, J.; Regmi, Y. N.; Leonard, B.; Fan, M. The Recent Progress and Future of Oxygen Reduction Reaction Catalysis: A Review. *Renewable Sustainable Energy Rev.* **2017**, *69*, 401−414.

(2) Van Spronsen, M. A.; Frenken, J. W. M.; Groot, I. M. N. Surface Science under Reaction Conditions: CO Oxidation on Pt and Pd Model Catalysts. *Chem. Soc. Rev.* **2017**, *46*, 4347.

(3) Deutschmann, O.; Knözinger, H.; Kochloefl, K.; Turek, T. Heterogeneous Catalysis and Solid Catalysts. *Ullmann's Encyclopedia of Industrial Chemistry* **2009**, *1*, 5−6.

(4) Quaino, P.; Juarez, F.; Santos, E.; Schmickler, W. Volcano Plots in Hydrogen Electrocatalysis-Uses and Abuses. *Beilstein J. Nanotechnol.* **2014**, *5*, 846−854.

(5) Pomerantseva, E.; Resini, C.; Kovnir, K.; Kolen'ko, Y. V. Emerging Nanostructured Electrode Materials for Water Electrolysis and Rechargeable beyond Li-Ion Batteries. *Advances in Physics: X.* **2017**, *2*, 211−253.

(6) Stephens, I. E. L.; Bondarenko, A. S.; Grønbjerg, U.; Rossmeisl, J.; Chorkendorff, I. Understanding the Electrocatalysis of Oxygen Reduction on Platinum and Its Alloys. *Energy Environ. Sci.* **2012**, *5*, 6744−6762.

(7) Greeley, J.; Stephens, I. E. L.; Bondarenko, A. S.; Johansson, T. P.; Hansen, H. A.; Jaramillo, T. F.; Rossmeisl, J.; Chorkendorff, I.; Nørskov, J. K. Alloys of Platinum and Early Transition Metals as Oxygen Reduction Electrocatalysts. *Nat. Chem.* **2009**, *1*, 552−556.

(8) Gutić, S. J.; Dobrota, A. S.; Fako, E.; Skorodumova, N. V.; López, N.; Pašti, I. A. Hydrogen Evolution Reaction-From Single Crystal to Single Atom Catalysts. *Catalysts* **2020**, *10*, 290.

(9) Sheng, W.; Myint, M.; Chen, J. G.; Yan, Y. Correlating the Hydrogen Evolution Reaction Activity in Alkaline Electrolytes with the Hydrogen Binding Energy on Monometallic Surfaces. *Energy Environ. Sci.* **2013**, *6*, 1509−1512.

(10) Xia, W.; Mahmood, A.; Liang, Z.; Zou, R.; Guo, S. Earth-Abundant Nanomaterials for Oxygen Reduction. *Angew. Chem., Int. Ed.* **2016**, *55*, 2650−2676.

(11) Xu, D.; Bliznakov, S.; Liu, Z.; Fang, J.; Dimitrov, N. Composition-Dependent Electrocatalytic Activity of Pt-Cu Nanocube Catalysts for Formic Acid Oxidation. *Angew. Chem., Int. Ed.* **2010**, *49*, 1282−1285.

(12) Koh, S.; Strasser, P. Electrocatalysis on Bimetallic Surfaces: Modifying Catalytic Reactivity for Oxygen Reduction by Voltammetric Surface Dealloying. *J. Am. Chem. Soc.* **2007**, *129*, 12624−12625.

(13) Xu, D.; Liu, Z.; Yang, H.; Liu, Q.; Zhang, J.; Fang, J.; Zou, S.; Sun, K. Solution-Based Evolution and Enhanced Methanol Oxidation Activity of Monodisperse Platinum-Copper Nanocubes. *Angew. Chem., Int. Ed.* **2009**, *48*, 4217−4221.

(14) Zhou, S.; Varughese, B.; Eichhorn, B.; Jackson, G.; McIlwrath, K. Pt−Cu Core−Shell and Alloy Nanoparticles for Heterogeneous NO_x Reduction: Anomalous Stability and Reactivity of a Core−Shell Nanostructure. *Angew. Chem., Int. Ed.* **2005**, *44*, 4539−4543.
(15) Kodama, K.; Nagai, T.; Kuwaki, A.; Jinnouchi, R.; Morimoto, Y. Challenges in Applying Highly Active Pt-Based Nanostructured Catalysts for Oxygen Reduction Reactions to Fuel Cell Vehicles. *Nat. Nanotechnol.* **2021**, *16*, 140−147.
(16) Zhao, Q.; Wang, C.; Wang, H.; Wang, J.; Tang, Y.; Mao, Z.; Sasaki, K. Synthesis of a High-Performance Low-Platinum PtAg/C Alloyed Oxygen Reduction Catalyst through the Gradual Reduction Method. *New J. Chem.* **2020**, *44*, 3728−3736.
(17) Filie, A.; Shirman, T.; Foucher, A. C.; Stach, E. A.; Aizenberg, M.; Aizenberg, J.; Friend, C. M.; Madix, R. J. Dilute Pd-in-Au Alloy RCT-SiO_2 Catalysts for Enhanced Oxidative Methanol Coupling. *J. Catal.* **2021**, *6*, 1−11.
(18) Ryoo, R.; Kim, J.; Jo, C.; Han, S. W.; Kim, J.-C.; Park, H.; Han, J.; Shin, H. S.; Shin, J. W. Rare-Earth-Platinum Alloy Nanoparticles in Mesoporous Zeolite for Catalysis. *Nature* **2020**, *585*, 221−224.
(19) Shao, M.; Chang, Q.; Dodelet, J.-P.; Chenitz, R. Recent Advances in Electrocatalysts for Oxygen Reduction Reaction. *Chem. Rev.* **2016**, *116*, 3594−3657.
(20) Yu, W.; Porosoff, M. D.; Chen, J. G. Review of Pt-Based Bimetallic Catalysis: From Model Surfaces to Supported Catalysts. *Chem. Rev.* **2012**, *112*, 5780−5817.
(21) Kuhl, S.; Gocyla, M.; Heyen, H.; Selve, S.; Heggen, M.; Dunin-Borkowski, R. E.; Strasser, P. Concave Curvature Facets Benefit Oxygen Electroreduction Catalysis on Octahedral Shaped PtNi Nanocatalysts. *J. Mater. Chem. A* **2019**, *7*, 1149−1159.
(22) Singh, A. K.; Xu, Q. Synergistic Catalysis over Bimetallic Alloy Nanoparticles. *ChemCatChem* **2013**, *5*, 652−676.
(23) Luneau, M.; Shirman, T.; Foucher, A. C.; Duanmu, K.; Verbart, D. M. A.; Sautet, P.; Stach, E. A.; Aizenberg, J.; Madix, R. J.; Friend, C. M. Achieving High Selectivity for Alkyne Hydrogenation at High Conversions with Compositionally Optimized PdAu Nanoparticle Catalysts in Raspberry Colloid-Templated SiO_2. *ACS Catal.* **2020**, *10*, 441−450.
(24) Luneau, M.; Guan, E.; Chen, W.; Foucher, A. C.; Marcella, N.; Shirman, T.; Verbart, D. M. A.; Aizenberg, J.; Aizenberg, M.; Stach, E. A.; Madix, R. J.; Frenkel, A. I.; Friend, C. M. Enhancing Catalytic Performance of Dilute Metal Alloy Nanomaterials. *Commun. Chem.* **2020**, *3*, 1−9.
(25) Cargnello, M.; Doan-Nguyen, V. V. T.; Gordon, T. R.; Diaz, R. E.; Stach, E. A.; Gorte, R. J.; Fornasiero, P.; Murray, C. B. Control of Metal Nanocrystal Size Reveals Metal-Support Interface Role for Ceria Catalysts. *Science* **2013**, *341*, 771−773.
(26) Jimenez, J. D.; Wen, C.; Lauterbach, J. Design of Highly Active Cobalt Catalysts for CO_2 Hydrogenation *via* the Tailoring of Surface Orientation of Nanostructures. *Catal. Sci. Technol.* **2019**, *9*, 1970−1978.
(27) Cao, S.; Tao, F.; Tang, Y.; Li, Y.; Yu, J. Size-and Shape-Dependent Catalytic Performances of Oxidation and Reduction Reactions on Nanocatalysts. *Chem. Soc. Rev.* **2016**, *45*, 4747.
(28) Wang, D.; Xin, H. L.; Hovden, R.; Wang, H.; Yu, Y.; Muller, D. A.; DiSalvo, F. J.; Abruña, H. D. Structurally Ordered Intermetallic Platinum−Cobalt Core−Shell Nanoparticles with Enhanced Activity and Stability as Oxygen Reduction Electrocatalysts. *Nat. Mater.* **2013**, *12* (1), 81−87.
(29) Liu, H.; Li, C.; Chen, D.; Cui, P.; Ye, F.; Yang, J. Uniformly Dispersed Platinum-Cobalt Alloy Nanoparticles with Stable Compositions on Carbon Substrates for Methanol Oxidation Reaction. *Sci. Rep.* **2017**, *7*, 1−8.
(30) Salvatore Aricó, A.; Stassi, A.; Gatto, I.; Monforte, G.; Passalacqua, E.; Antonucci, V. Surface Properties of Pt and PtCo Electrocatalysts and Their Influence on the Performance and Degradation of High-Temperature Polymer Electrolyte Fuel Cells. *J. Phys. Chem. C* **2010**, *114*, 15823−15836.
(31) Chen, H. Y.; Niu, H. J.; Ma, X.; Feng, J. J.; Weng, X.; Huang, H.; Wang, A. J. Flower-Like Platinum-Cobalt-Ruthenium Alloy Nanoassemblies as Robust and Highly Efficient Electrocatalyst for Hydrogen Evolution Reaction. *J. Colloid Interface Sci.* **2020**, *561*, 372−378.
(32) Xin, H. L.; Mundy, J. A.; Liu, Z.; Cabezas, R.; Hovden, R.; Kourkoutis, L. F.; Zhang, J.; Subramanian, N. P.; Makharia, R.; Wagner, F. T.; Muller, D. A. Atomic-Resolution Spectroscopic Imaging of Ensembles of Nanocatalyst Particles across the Life of a Fuel Cell. *Nano Lett.* **2012**, *12*, 490−497.
(33) Ismail, A. S. M.; Casavola, M.; Liu, B.; Gloter, A.; Van Deelen, T. W.; Versluijs, M.; Meeldijk, J. D.; Stéphan, O.; De Jong, K. P.; De Groot, F. M. F. Atomic-Scale Investigation of the Structural and Electronic Properties of Cobalt-Iron Bimetallic Fischer−Tropsch Catalysts. *ACS Catal.* **2019**, *9*, 7998−8011.
(34) Wang, C.; Van Der Vliet, D.; Chang, K. C.; You, H.; Strmcnik, D.; Schlueter, J. A.; Markovic, N. M.; Stamenkovic, V. R. Monodisperse Pt3Co Nanoparticles as a Catalyst for the Oxygen Reduction Reaction: Size-Dependent Activity. *J. Phys. Chem. C* **2009**, *113*, 19365−19368.
(35) Xiong, Y.; Xiao, L.; Yang, Y.; Disalvo, F. J.; Abruña, H. D. High-Loading Intermetallic Pt_3Co/C Core-Shell Nanoparticles as Enhanced Activity Electrocatalysts toward the Oxygen Reduction Reaction (ORR). *Chem. Mater.* **2018**, *30*, 1532−1539.
(36) Lee, J. D.; Jishkariani, D.; Zhao, Y.; Najmr, S.; Rosen, D.; Kikkawa, J. M.; Stach, E. A.; Murray, C. B. Tuning the Electrocatalytic Oxygen Reduction Reaction Activity of Pt-Co Nanocrystals by Cobalt Concentration with Atomic-Scale Understanding. *ACS Appl. Mater. Interfaces* **2019**, *11*, 26789−26797.
(37) Jung, N.; Bhattacharjee, S.; Gautam, S.; Park, H.-Y.; Ryu, J.; Chung, Y.-H.; Lee, S.-Y.; Jang, I.; Jang, J. H.; Park, S. H.; Chung, D. Y.; Sung, Y.-E.; Chae, K.-H.; Waghmare, U. V.; Lee, S.-C.; Yoo, S. J. Organic-Inorganic Hybrid PtCo Nanoparticle with High Electrocatalytic Activity and Durability for Oxygen Reduction. *NPG Asia Mater.* **2016**, *8*, 237.
(38) Wang, Y.-J.; Zhao, N.; Fang, B.; Li, H.; Bi, X. T.; Wang, H. A Highly Efficient PtCo/C Electrocatalyst for the Oxygen Reduction Reaction. *RSC Adv.* **2016**, *6*, 34484−34491.
(39) Myint, M. N. Z.; Yan, B.; Wan, J.; Zhao, S.; Chen, J. G. Reforming and Oxidative Dehydrogenation of Ethane with CO_2 as a Soft Oxidant over Bimetallic Catalysts. *J. Catal.* **2016**, *343*, 168−177.
(40) Jia, Q.; Caldwell, K.; Strickland, K.; Ziegelbauer, J. M.; Liu, Z.; Yu, Z.; Ramaker, D. E.; Mukerjee, S. Improved Oxygen Reduction Activity and Durability of Dealloyed PtCox Catalysts for Proton Exchange Membrane Fuel Cells: Strain, Ligand, and Particle Size Effects. *ACS Catal.* **2015**, *5*, 176−186.
(41) Boyaci San, F. G.; Dursun, S.; Yazici, M. S. PtCo on Continuous-Phase Graphene as PEM Fuel Cell Catalyst. *Int. J. Energy Res.* **2021**, *45*, 1673−1684.
(42) Lee, H.; Lim, J.; Lee, C.; Back, S.; An, K.; Shin, J. W.; Ryoo, R.; Jung, Y.; Park, J. Y. Boosting Hot Electron Flux and Catalytic Activity at Metal−Oxide Interfaces of PtCo Bimetallic Nanoparticles. *Nat. Commun.* **2018**, *9*, 1−8.
(43) Farkaš, B.; Perry, C. B.; Jones, G.; De Leeuw, N. H. Adsorbate-Induced Segregation of Cobalt from PtCo Nanoparticles: Modeling Au Doping and Core AuCo Alloying for the Improvement of Fuel Cell Cathode Catalysts. *J. Phys. Chem. C* **2020**, *124*, 18321−18334.
(44) Yu, Z.; Zhang, J.; Liu, Z.; Ziegelbauer, J. M.; Xin, H.; Muller, D. A.; Wagner, F. T. Comparison between Dealloyed $PtCo_3$ and $PtCu_3$ Cathode Catalysts for Proton Exchange Membrane Fuel Cells. *J. Phys. Chem. C* **2012**, *116*, 19877−19885.
(45) Liu, Z.; Lei, Y.; Wang, G. First-Principles Computation of Surface Segregation in L10 CoPt Magnetic Nanoparticles. *J. Phys.: Condens. Matter* **2016**, *28*, 266002.
(46) Sun, X.; Jia, Z. Y.; Huang, Y. H.; Harrell, J. W.; Nikles, D. E.; Sun, K.; Wang, L. M. Synthesis and Magnetic Properties of CoPt Nanoparticles. *J. Appl. Phys.* **2004**, *95*, 6747.
(47) Karipoth, P.; Joseyphus, R. J. Evolution of High Coercivity in CoPt Nanoparticles Through Nitrogen Assisted Annealing. *J. Supercond. Novel Magn.* **2014**, *27*, 2123−2130.

https://doi.org/10.1021/acsnano.1c09450
ACS Nano 2021, 15, 20619−20632

(48) Luo, J.; Yun, H.; Mironenko, A. V.; Goulas, K.; Lee, J. D.; Monai, M.; Wang, C.; Vorotnikov, V.; Murray, C. B.; Vlachos, D. G.; Fornasiero, P.; Gorte, R. J. Mechanisms for High Selectivity in the Hydrodeoxygenation of 5-Hydroxymethylfurfural over PtCo Nanocrystals. *ACS Catal.* **2016**, *6*, 4095−4104.
(49) Wang, C.; Luo, J.; Liao, V.; Lee, J. D.; Onn, T. M.; Murray, C. B.; Gorte, R. J. A Comparison of Furfural Hydrodeoxygenation over Pt-Co and Ni-Fe Catalysts at High and Low H_2 Pressures. *Catal. Today* **2018**, *302*, 73−79.
(50) Zhao, S.; Li, Y.; Stavitski, E.; Tappero, R.; Crowley, S.; Castaldi, M. J.; Zakharov, D. N.; Nuzzo, R. G.; Frenkel, A. I.; Stach, E. A. Operando Characterization of Catalysts through Use of a Portable Microreactor. *ChemCatChem* **2015**, *7*, 3683−3691.
(51) Zhao, S.; Li, Y.; Liu, D.; Liu, J.; Liu, Y.-M.; Zakharov, D. N.; Wu, Q.; Orlov, A.; Gewirth, A. A.; Stach, E. A.; Nuzzo, R. G.; Frenkel, A. I. Multimodal Study of the Speciations and Activities of Supported Pd Catalysts during the Hydrogenation of Ethylene. *J. Phys. Chem. C* **2017**, *121*, 18962−18972.
(52) Li, L.; Wang, L. L.; Johnson, D. D.; Zhang, Z.; Sanchez, S. I.; Kang, J. H.; Nuzzo, R. G.; Wang, Q.; Frenkel, A. I.; Li, J.; Ciston, J.; Stach, E. A.; Yang, J. C. Noncrystalline-to-Crystalline Transformations in Pt Nanoparticles. *J. Am. Chem. Soc.* **2013**, *135*, 13062−13072.
(53) Liu, D.; Li, Y.; Kottwitz, M.; Yan, B.; Yao, S.; Gamalski, A.; Grolimund, D.; Safonova, O. V.; Nachtegaal, M.; Chen, J. G.; Stach, E. A.; Nuzzo, R. G.; Frenkel, A. I. Identifying Dynamic Structural Changes of Active Sites in Pt−Ni Bimetallic Catalysts Using Multimodal Approaches. *ACS Catal.* **2018**, *8*, 4120−4131.
(54) Li, Y.; Zakharov, D.; Zhao, S.; Tappero, R.; Jung, U.; Elsen, A.; Baumann, P.; Nuzzo, R. G.; Stach, E. A.; Frenkel, A. I. Complex Structural Dynamics of Nanocatalysts Revealed in Operando Conditions by Correlated Imaging and Spectroscopy Probes. *Nat. Commun.* **2015**, *6*, 1−6.
(55) Krivanek, O. L.; Chisholm, M. F.; Nicolosi, V.; Pennycook, T. J.; Corbin, G. J.; Dellby, N.; Murfitt, M. F.; Own, C. S.; Szilagyi, Z. S.; Oxley, M. P.; Pantelides, S. T.; Pennycook, S. J. Atom-by-Atom Structural and Chemical Analysis by Annular Dark-Field Electron Microscopy. *Nature* **2010**, *464*, 571−574.
(56) Cesar, L. G.; Yang, C.; Lu, Z.; Ren, Y.; Zhang, G.; Miller, J. T. Identification of a Pt_3Co Surface Intermetallic Alloy in Pt−Co Propane Dehydrogenation Catalysts. *ACS Catal.* **2019**, *9*, 5231−5244.
(57) Front, A.; Legrand, B.; Tréglia, G.; Mottet, C. Bidimensional Phases in Co−Pt Surface Alloys: A Theoretical Study of Ordering and Surface Segregation. *Surf. Sci.* **2019**, *679*, 128−138.
(58) Ward, M.R.; Theobald, B.; Sharman, J.; Boyes, E.D.; Gai, P.L. Direct Observations of Dynamic PtCo Interactions in Fuel Cell Catalyst Precursors at the Atomic Level Using E(S)TEM. *J. Microsc.* **2018**, *269*, 143−150.
(59) Farkaš, B.; Perry, C. B.; Jones, G.; de Leeuw, N. H. Adsorbate-Induced Segregation of Cobalt from PtCo Nanoparticles: Modeling Au Doping and Core AuCo Alloying for the Improvement of Fuel Cell Cathode Catalysts. *J. Phys. Chem. C* **2020**, *124*, 18321−18334.
(60) Xu, Q.; Kreidler, E.; He, T. Performance and Durability of PtCo Alloy Catalysts for Oxygen Electroreduction in Acidic Environments. *Electrochim. Acta* **2010**, *55*, 7551−7557.
(61) He, S.; Liu, Y.; Zhan, H.; Guan, L. Direct Thermal Annealing Synthesis of Ordered Pt Alloy Nanoparticles Coated with a Thin N-Doped Carbon Shell for the Oxygen Reduction Reaction. *ACS Catal.* **2021**, *11*, 9355−9365.
(62) Luo, J.; Yun, H.; Mironenko, A. V.; Goulas, K.; Lee, J. D.; Monai, M.; Wang, C.; Vorotnikov, V.; Murray, C. B.; Vlachos, D. G.; Fornasiero, P.; Gorte, R. J. Mechanisms for High Selectivity in the Hydrodeoxygenation of 5-Hydroxymethylfurfural over PtCo Nanocrystals. *ACS Catal.* **2016**, *6*, 4095−4104.
(63) Zhong, L.; Barreau, M.; Caps, V.; Papaefthimiou, V.; Haevecker, M.; Teschner, D.; Baaziz, W.; Borfecchia, E.; Braglia, L.; Zafeiratos, S. Improving the Catalytic Performance of Cobalt for CO Preferential Oxidation by Stabilizing the Active Phase through Vanadium Promotion. *ACS Catal.* **2021**, *11*, 5369−5385.
(64) Bi, W.; Fuller, T. Temperature Effects on PEM Fuel Cells Pt/C Catalyst Degradation. *ECS Trans.* **2007**, *11*, 1235.
(65) Chi, M.; Wang, C.; Lei, Y.; Wang, G.; Li, D.; More, K. L.; Lupini, A.; Allard, L. F.; Markovic, N. M.; Stamenkovic, V. R. Surface Faceting and Elemental Diffusion Behaviour at Atomic Scale for Alloy Nanoparticles during *in Situ* Annealing. *Nat. Commun.* **2015**, *6*, 1−9.
(66) Yang, F.; Wang, H.; Wang, H.; Zhang, J.; Zhu, J.; Li, Q.; Jiang, Y. Effect of Hydrogen Annealing on L10 Ordering Transformation and Magnetic Properties of CoPt Thin Films on B4C Underlayer. *J. Phys. D: Appl. Phys.* **2009**, *42*, 115001.
(67) Kong, F.-C.; Li, Y.-F.; Shang, C.; Liu, Z.-P. Stability and Phase Transition of Cobalt Oxide Phases by Machine Learning Global Potential Energy Surface. *J. Phys. Chem. C* **2019**, *123*, 17539−17547.
(68) Żyła, M.; Smoła, G.; Knapik, A.; Rysz, J.; Sitarz, M.; Grzesik, Z. The Formation of the Co_3O_4 Cobalt Oxide within CoO Substrate. *Corros. Sci.* **2016**, *112*, 536−541.
(69) Kale, G. M.; Pandit, S. S.; Jacob, K. T. Thermodynamics of Cobalt (II, III) Oxide (Co_3O_4): Evidence of Phase Transition. *Trans. Jpn. Inst. Met.* **1988**, *29*, 125−132.
(70) Hwang, S.; Kim, S. M.; Bak, S.-M.; Kim, S. Y.; Cho, B.-W.; Chung, K. Y.; Lee, J. Y.; Stach, E. A.; Chang, W. Using Real-Time Electron Microscopy to Explore the Effects of Transition-Metal Composition on the Local Thermal Stability in Charged $Li_xNi_yMn_zCo_{1-y-z}O_2$ Cathode Materials. *Chem. Mater.* **2015**, *27*, 3927−3935.
(71) Karki, K.; Huang, Y.; Hwang, S.; Gamalski, A. D.; Whittingham, M. S.; Zhou, G.; Stach, E. A. Tuning the Activity of Oxygen in $LiNi_{0.8}Co_{0.15}Al_{0.05}O_2$ Battery Electrodes. *ACS Appl. Mater. Interfaces* **2016**, *8*, 27762−27771.
(72) Jin, Y.; Xu, H.; Datye, A. K. Electron Energy Loss Spectroscopy (EELS) of Iron Fischer−Tropsch Catalysts. *Microsc. Microanal.* **2006**, *12*, 124−134.
(73) Lee, S. A.; Jeong, H.; Woo, S.; Hwang, J.-Y.; Choi, S.-Y.; Kim, S.-D.; Choi, M.; Roh, S.; Yu, H.; Hwang, J.; Kim, S. W.; Choi, W. S. Phase Transitions *via* Selective Elemental Vacancy Engineering in Complex Oxide Thin Films. *Sci. Reports* **2016**, *6*, 1−10.
(74) Kong, F.-C.; Li, Y.-F.; Shang, C.; Liu, Z.-P. Stability and Phase Transition of Cobalt Oxide Phases by Machine Learning Global Potential Energy Surface. *J. Phys. Chem. C* **2019**, *123*, 17539−17547.
(75) Stach, E.; Hwang, S.; Karki, K.; Kim, S.; Chang, W.; Chung, K.; Zhuo, G.; Yang, Q.; Whittingham, M. Using In-Situ Methods to Characterize Phase Changes in Charged Lithium Nickel Cobalt Aluminum Oxide Cathode Materials. *Microsc. Microanal.* **2019**, *25*, 2030−2031.
(76) Córdoba, R.; Fernández-Pacheco, R.; Fernández-Pacheco, A.; Gloter, A.; Magén, C.; Stéphan, O.; Ibarra, M. R.; De Teresa, J. M. Nanoscale Chemical and Structural Study of Co-Based FEBID Structures by STEM-EELS and HRTEM. *Nanoscale Res. Lett.* **2011**, *6*, 1−6.
(77) Zhao, Y.; Feltes, T. E.; Regalbuto, J. R.; Meyer, R. J.; Klie, R. F. *In Situ* Electron Energy Loss Spectroscopy Study of Metallic Co and Co Oxides. *J. Appl. Phys.* **2010**, *108*, 63704.
(78) Hart, J. L.; Lang, A. C.; Leff, A. C.; Longo, P.; Trevor, C.; Twesten, R. D.; Taheri, M. L. Direct Detection Electron Energy-Loss Spectroscopy: A Method to Push the Limits of Resolution and Sensitivity. *Sci. Rep.* **2017**, *7*, 1−14.
(79) Hart, J. L.; Lang, A. C.; Li, Y.; Hantanasirisakul, K.; Frenkel, A. I.; Taheri, M. L. A Synchrotron in the TEM: Spatially Resolved Fine Structure Spectra at High Energies. *arXiv*, 1909.06323, [cond-mat.mtrl-sci], https://arxiv.org/abs/1909.06323, (accessed Nov. 7, 2021).
(80) Zugic, B.; Wang, L.; Heine, C.; Zakharov, D. N.; Lechner, B. A. J.; Stach, E. A.; Biener, J.; Salmeron, M.; Madix, R. J.; Friend, C. M. Dynamic Restructuring Drives Catalytic Activity on Nanoporous Gold-Silver Alloy Catalysts. *Nat. Mater.* **2017**, *16*, 558−564.
(81) Mao, X.; Foucher, A. C.; Montini, T.; Stach, E. A.; Fornasiero, P.; Gorte, R. J. Epitaxial and Strong Support Interactions between Pt and $LaFeO_3$Films Stabilize Pt Dispersion. *J. Am. Chem. Soc.* **2020**, *142*, 10373−10382.

https://doi.org/10.1021/acsnano.1c09450
ACS Nano 2021, 15, 20619−20632

(82) Suenaga, K.; Okazaki, T.; Okunishi, E.; Matsumura, S. Detection of Photons Emitted from Single Erbium Atoms in Energy-Dispersive X-Ray Spectroscopy. *Nat. Photonics* **2012**, *6*, 545−548.
(83) Jungjohann, K.; Carter, C. B. *In Situ* and *Operando*. In *Transmission Electron Microscopy*; Springer International Publishing: Berlin-Heidelberg, 2016; pp 17−80.

https://doi.org/10.1021/acsnano.1c09450
ACS Nano 2021, 15, 20619−20632